

## Full length article

Coexistence of rhombohedral and orthorhombic phases in ultrathin BiFeO<sub>3</sub> films driven by interfacial oxygen octahedral couplingM.J. Han<sup>a,b</sup>, Y.J. Wang<sup>a</sup>, D.S. Ma<sup>c</sup>, Y.L. Zhu<sup>a,\*</sup>, Y.L. Tang<sup>a</sup>, Y. Liu<sup>a,b</sup>, N.B. Zhang<sup>a</sup>, J.Y. Ma<sup>a,d</sup>, X.L. Ma<sup>a,d</sup><sup>a</sup> Shenyang National Laboratory for Materials Science, Institute of Metal Research, Chinese Academy of Sciences, Wenhua Road 72, 110016 Shenyang, China<sup>b</sup> University of Chinese Academy of Sciences, Yuquan Road 19, 100049 Beijing, China<sup>c</sup> School of Physics, Nankai University, Weijin Road 94, 300071 Tianjin, China<sup>d</sup> School of Materials Sciences and Engineering, Lanzhou University of Technology, Langongping Road 287, 730050 Lanzhou, China

## ARTICLE INFO

## Article history:

Received 25 August 2017

Received in revised form

28 November 2017

Accepted 1 December 2017

Available online 20 December 2017

## Keywords:

Phase transition

BiFeO<sub>3</sub>

Oxygen octahedral coupling

Transmission electron microscopy

First-principles calculation

## ABSTRACT

Coexistence of two phases creates a morphotropic phase boundary in perovskite oxides, which can provide large piezoelectric response, generating it a well suited system for probe-based memories and actuator applications. The coexistence of two phases in thin films is proposed to be induced by epitaxial constraints from substrates or chemical compositional modifications by substitution. In this work, we found a new formation mechanism of two-phase coexistence driven by interfacial oxygen octahedral coupling (OOC) in oxide heterostructures. We fabricated a series of BiFeO<sub>3</sub> (BFO) ultrathin films on various orthorhombic substrates exerting from tensile to compressive strains by Pulsed Laser Deposition (PLD) techniques. Aberration-corrected transmission electron microscopy demonstrates that the lattice rotation and oxygen octahedral rotation (OOR) patterns transfer from these substrates to BFO films in about 3 unit cells while an orthorhombic (*Pnma*) phase forms at the interface due to OOC. This *Pnma* phase is non-polar, which differs from polar phases of *Ima2* or *Pmc2<sub>1</sub>* when a large tensile strain is imposed onto BFO. First-principles calculations reproduce these experimental results perfectly. This phase transition occurs when BFO films are under both tensile and compressive strains suggesting that OOC alone can induce phase transition in ultrathin BFO films. Such coexistence of two phases may have many potential applications in the field of electronics, such as ferroelectric sensors and actuators.

© 2017 Acta Materialia Inc. Published by Elsevier Ltd. All rights reserved.

## 1. Introduction

Perovskite ferroelectric films have long been an intriguing topic because slight adjustments of atomic structures can bring large physical response and generate multiple functionalities [1,2]. Such functionalities have potential applications in memory devices, spintronics and sensors [1,3–5]. Among them, Bismuth Ferrite (BiFeO<sub>3</sub> or BFO) has been a topic of intense interest since the last two decades because it is the only material that possesses both antiferromagnetic and strong ferroelectric orders simultaneously at room temperature so far. The structure of BFO is rhombohedral with its space group *R3c*, which can be characterized by two distorted perovskite blocks with  $a_{pc} = 3.96 \text{ \AA}$  and  $\alpha_{pc} = 89.46^\circ$  [6,7]. BFO shows both ferroelectric order and G-type antiferromagnetic

order at room temperature, the corresponding transition temperatures being  $T_C \sim 1103 \text{ K}$  and  $T_N \sim 643 \text{ K}$ , respectively [8]. In addition to these facts, the structure of BFO is very flexible, making it possible to tune its structural parameters to accommodate over a wide range of epitaxial strain (more than  $\pm 4\%$ ) which may come from the ‘willingness’ rotation of oxygen octahedra [3,9,10]. In particular, when there are two phases coexistence in the film, it may produce large piezoelectric response and have potential utilization in probe-based data storage and actuators [11–13].

Usually, the approach to two phases acquisition in thin films is through epitaxial constraints [11] or by changing the chemical composition [13]. When BFO is imposed to a strain, an evolution of phase transition: ‘Tetragonal  $\rightarrow M_C \rightarrow M_A \rightarrow$  Rhombohedral  $\rightarrow M_B \rightarrow$  Orthorhombic’ (*M* stands for monoclinic) caused by a switch from large compressive strain to tensile strain has been generally accepted [3,12]. As we can see, the coexistence of two phases may occur at a critical strain value. Apart from strain engineering, the crystal structure of BFO film can also be altered by the change of

\* Corresponding author.

E-mail address: [ylzhu@imr.ac.cn](mailto:ylzhu@imr.ac.cn) (Y.L. Zhu).

chemical composition. It was reported that when the composition of Sm is about 14%, the samarium-substituted BFO film shows high dielectric constant ( $\sim 400$ ) and  $d_{33}$  ( $\sim 100 \text{ pmV}^{-1}$ ), with the hysteresis loop changing from a standard ferroelectric shape to a double hysteresis loop [13]. Subsequent studies show these changes come from the formation of a nanoscale mixture of polar rhombohedral and non-polar orthorhombic structures [14–16].

The methods above are long-range effects and lack atomic range control. However, as a contrast, OOC at heterostructural interfaces can produce a route to controlling OOR at atomic scale and finally tunes the functionality in the film. Benefited from the progress in Sub-angstrom Transmission Electron Microscopy, especially the development of Negative Spherical-Aberration ( $C_s$ ) Imaging (NCSI) [17] and Annular Bright-Field (ABF) imaging [18,19], oxygen positions can be easily extracted in high-resolution images [20,21]. As a result, it is possible for us to discover the relationship between the changing of  $\text{BO}_6$  octahedra and its associated functionalities at atomic scale [22,23]. The changing of OOR may alter the electronic bandgap [24], thermal conductivity [25], optical, ferroelectric and magnetic properties, etc [26,27]. Besides, there exists an oxygen octahedral proximity effect at heterostructure interfaces due to the corner-connectivity of  $\text{BO}_6$  octahedra, which enables OOR to transfer from substrates to films [28]. The interfacial OOC may spatially localize the non-equilibrium octahedral rotation behavior and cause changes in magnetic anisotropy [29,30]. The control of OOR in perovskite oxide heterostructures has been an emerging route to structural and functional modulation. It is short-ranged (about 2 nm) [31–33], allowing us to control the functionalities at an atomic level.

In this work, we deposited a series of ultrathin (about 6–7 unit cells) BFO films on various orthorhombic perovskite substrates which provide both tensile and compressive strains. All of the substrates possess  $Pnma$  space group. There exists a crystal symmetry mismatch (i.e. OOR mismatch) between BFO and orthorhombic substrates. Experimental and theoretical results indicate that a phase transition of BFO from polar rhombohedral to non-polar orthorhombic structure occurs near the interface in the range of about 3 unit cells, whereas BFO still possesses rhombohedral structure near the surface. Further study has confirmed that OOC plays the main role in this phase transition.

## 2. Experimental and calculational methods

We fabricated a series of heterostructures by depositing 2–3 nm-thick BFO epitaxial thin films on  $(110)_{\text{ortho}}$ -oriented (The subscript “ortho” denotes *orthorhombic perovskite notation*) substrates ( $\text{NdGaO}_3$  (NGO),  $\text{DyScO}_3$  (DSO),  $\text{GdScO}_3$  (GSO),  $\text{NdScO}_3$  (NSO) and  $\text{PrScO}_3$  (PSO)) using Pulsed Laser Deposition (PLD) method. The excimer laser is 248 nm KrF. Before deposition, these substrates were heated up to  $850^\circ\text{C}$  for 20 min in order to clean the surface and then cooled down to  $800^\circ\text{C}$ . BFO target (1 mol% Bi-riched) was pre-sputtered for 15 min to clean its surface. Throughout the deposition process, an oxygen pressure of 12 Pa, a repetition rate of 6 Hz, and a laser energy density of  $2 \text{ J} \cdot \text{cm}^{-2}$  were applied. After deposition, these samples were stabilized at  $800^\circ\text{C}$  for 5 min and then cooled down to room temperature at a cooling rate of  $5^\circ\text{C} \cdot \text{min}^{-1}$  in an oxygen pressure of  $3 \times 10^4 \text{ Pa}$ .

Specimens used for cross-sectional observations were prepared by traditional method: slicing, gluing, grinding, dimpling and ion milling. A Gatan 691 PIPS was used for ion milling. High-angle annular dark field (HAADF) and Annular Bright-Field (ABF) images were acquired using aberration-corrected scanning transmission electron microscope (Titan Cubed 60–300 kV microscope (FEI)). The microscope is fitted with a high-brightness field-emission gun and double aberration ( $C_s$ ) correctors from CEOS

operating at 300 kV.

A Wiener filter of HAADF and ABF images and a low-pass annular mask restricted to the instrument resolution limit of the images were used in order to reduce the noise in the obtained images. By using a two dimensional (2D) Gaussian peaks fitting in Matlab [34], the atom positions can be accurately determined [35], thus making it possible to acquire the lattice spacing, B-site ion displacement and oxygen rotation angle.

First-principles calculations of the BFO/NGO interface were performed using the VASP code [36,37]. The generalized gradient approximation exchange–correlation functional was used with projector-augmented wave method [38]. The plane wave cutoff energy was 500 eV. The O 2s2p, Fe 3d4s, Bi 5d6s6p, Ga 4s4p, and Nd 5s5p4f6s electrons were treated as valence electrons. The Hubbard U correction was applied on the 3d and 4f electrons of Fe ( $U_{\text{eff}} = 3.8 \text{ eV}$ ) [39] and Nd ( $U_{\text{eff}} = 9 \text{ eV}$ ) [40]. The antiferromagnetic orders of BFO and NGO were set at G-type and A-type: The Fe ions are ferromagnetically coupled in (111) planes and antiferromagnetically coupled between adjacent (111) planes, while the specific plane of Nd ions is the (100) plane.

## 3. Results and discussions

The crystal symmetry of perovskites can be described by the pattern of the OOR using the Glazer notation [41]. Fig. 1(a) is the schematic model of  $\text{BO}_6$  octahedral rotation in one pseudo-cubic unit cell. The rotation angle of one oxygen octahedron can be decomposed into three components along  $a$ ,  $b$  and  $c$  axes in the rectangular coordinate system. The magnitudes of the three components are symbolically indicated by a set of three letters (such as  $aaa$  or  $abc$ ), and the superscripts “+”, “-” and “0” are used to represent in-phase, out-of-phase and no rotation along the corresponding axes. According to this rule, the symmetry of BFO and NGO can be described by the symbols  $a^-a^-a^-$  and  $b^+a^-a^-$ , respectively, as shown in Fig. 1(b). The  $a$ ,  $b$  and  $c$  axes in Fig. 1 correspond to [001], [1–10] and [110] in the orthogonal system, respectively. There exists an out-of-phase/in-phase rotation mismatch between BFO and NGO when projected along the  $a$ -axis of BFO, which can be quantitatively described by the B-O-B Bond Angle ( $\theta$ ), as shown in the left panel of Fig. 1(b). Another mismatch is characterized by the Horizontal Lattice Rotation Angle ( $\alpha$ ) when projected along the  $b$ -axis of BFO, as shown in the right panel of Fig. 1(b).

Fig. 2 (a) is a high resolution HAADF image of the BFO/NGO heterostructure along the  $a$ -axis. The thickness of the epitaxial BFO film is about 6–7 unit cells. Fig. 2(b) is the Fast Fourier Transformation (FFT) of the blue rectangle in Fig. 2(a), where the appearance of weak half-order peaks (white squares in (b))

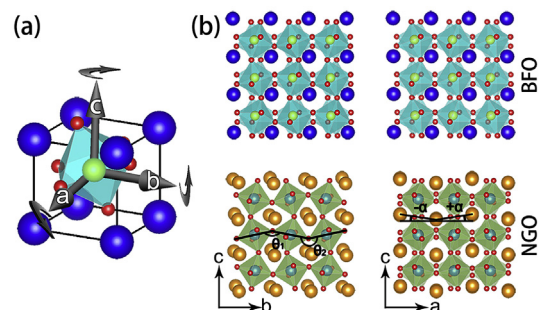


**Fig. 1.** Schematics of oxygen octahedral rotation ordering. (a) The oxygen rotation model in one pseudo-cubic unit cell. (b) Schematic models of BFO ( $a^-a^-a^-$ ) and NGO ( $b^+a^-a^-$ ) crystal structures along [100] (left) and [010] (right) directions.  $\theta_1$  and  $\theta_2$  represent In-plane B-O-B Bond Angles,  $\alpha$  represents the Horizontal Lattice Rotation Angle.

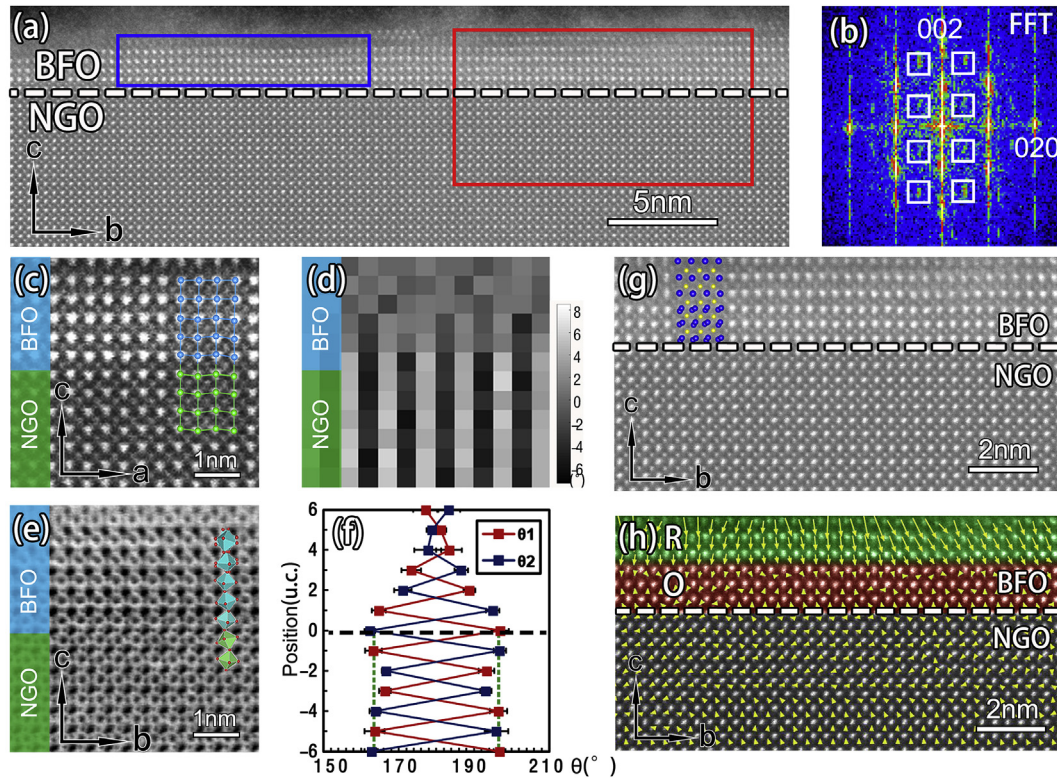


**Fig. 2.** Phase transition at the interface in the BFO/NGO heterostructure. (a) An atomic resolution HAADF image of the BFO/NGO interface along  $a$ -axis. (b) The Fast Fourier Transformation (FFT) of the blue rectangle in (a). These half-order peaks (white squares in (b)) suggest the occurrence of a phase transition from rhombohedral to orthorhombic structure in the BFO film. (c) An atomic resolution HAADF image of BFO/NGO along  $b$ -axis. (d) The 2-D mapping of the Horizontal Lattice Rotation Angle ( $\alpha$ ) of (c). (e) An ABF image of BFO/NGO system taken along  $a$ -axis of BFO. (f) The Layer-position-dependent mean In-plane B-O-B Bond Angle ( $\theta$ ) of (e), in which red squares denote  $\theta_1$  and blue squares denote  $\theta_2$ , the error bar of each square corresponding to the standard deviation of the octahedral tilt angle. The green dot lines corresponding to the angle  $\theta$  of bulk NGO. (g) An enlarged image of the red rectangle in (a). Schematic unit cells are overlapped on the images: Bi – blue circles, Fe – yellow circles. (h) B-site ion displacements of (g), confirming the coexistence of rhombohedral and orthorhombic structures in the BFO film. The upper green area denotes the rhombohedral structure whereas the lower red area denotes the orthorhombic structure. (For interpretation of the references to colour in this figure legend, the reader is referred to the Web version of this article.)

represents the signature of an orthorhombic symmetry. The FFT data indicate that there may exist a phase transition from rhombohedral to orthorhombic in the BFO film.

To make it clear whether the whole BFO film does transform to orthorhombic structure, lattice rotation and OOR of the BFO/NGO heterostructure are analyzed. Fig. 2(c) is an atomic resolution HAADF image of the BFO/NGO heterostructure projected along  $b$ -axis of BFO. Fig. 2(d) is a 2-D distribution of Horizontal Lattice Rotation Angle ( $\alpha$ ) according to the atom positions in Fig. 2(c) refined by Gaussian peak fitting in Matlab. From the model of NGO projected along  $b$ -axis (right panel of Fig. 1 (b)) we can see that if the angle  $\alpha$  of one unit cell is positive, then both the angles of the left and right unit cells are negative, whereas those of the up and down unit cells are positive. As a result, a stripe-like distribution of the angle  $\alpha$  appears in NGO. In the case of BFO, the angle  $\alpha$  of each unit cell is almost zero degree. From Fig. 2(d), we can see that the angle  $\alpha$  in the BFO film near the BFO/NGO interface also shows a stripe-like distribution. The range of this distribution is about 3 unit cells. This is the evidence of A-site ion displacements in BFO due to crystal symmetry mismatch. To find out OOR in the BFO/NGO heterostructure, we obtained an ABF image along  $a$ -axis of BFO, as shown in Fig. 2(e), with BFO and NGO shows out-of-phase and in-phase OOR, respectively. In this image, oxygen atomic columns are clearly visible, thus Gaussian peak fitting can be used to acquire oxygen column position in both BFO and NGO. Fig. 2(f) shows the variation of In-plane B-O-B Bond Angle ( $\theta$ ) ( $B = \text{Ga}, \text{Fe}$ ) as a function of their coordinates of B ions in the  $c$  axis. The angle  $\theta$  in the initial

three unit cells in BFO near the interface is strongly affected by the substrate. In the upper layer of BFO, the oxygen columns become dispersed because of the out-of-phase rotation, accounting for the angle  $\theta$  of each unit cell being almost  $180^\circ$ . This indicates the OOR propagates from the NGO substrate into the BFO film in about 3 unit cells. Combined with the evidence of half-order peaks in Fig. 2(b), the high-resolution images suggest that the BFO unit cells near the interface should become  $Pnma$ , the same as the NGO substrate. For the BFO unit cells near the film surface, both the distributions of the angles  $\alpha$  and  $\theta$  indicate that BFO still possesses the rhombohedral structure. The tetragonality of the BFO film is also calculated to exclude the existence of the tetragonal phase. The largest tetragonality of BFO is about 1.11 at the surface, rather smaller than the tetragonal structure of 1.27. Therefore, there exist two phases in this ultra-thin BFO film, one being ferroelectric rhombohedral structure near the surface while the other paraelectric  $Pnma$  at BFO/NGO interface. The coexistence of the two phases is illustrated in Fig. 2(g) and (h). Fig. 2(h) is the enlarged image of the red rectangle in (a). Fig. 2(h) gives the B-site ionic displacements relative to the central positions of the four nearest A-site ions. It is clear that the red area with no ionic displacement corresponds to the  $Pnma$  phase, while the green area with both in-plane and out-of-plane ion displacements corresponds to the rhombohedral structure. Notice that the out-of-plane displacements are larger than the in-plane ones, since the NGO substrate applies a compressive epitaxial strain to the BFO film. In another way, the top surface of BFO film may adsorb some negatively charged molecules ( $\text{O}^{2-}$ ,  $\text{OH}^-$  etc) which help screen the

depolarization field and enhance the out-of-plane polarization.

To demonstrate that there is a two-phase coexistence in the BFO ultrathin film, we performed first-principles calculations, as shown in Fig. 3. The BFO/NGO interface model was constructed by packing three layers of NGO unit cells and six layers of BFO unit cells with a vacuum layer of 20 Å. The bottom NGO unit cell was fixed to simulate the effect of substrate and all other atoms were allowed to relax. In the initial state, the three BFO layers adjacent with NGO were forced to adopt the  $b^+a^-a^-$  symmetry, while the other three BFO layers still possess the  $a^-a^-a^-$  symmetry. In the optimized structure, there exists a clear division of the two areas in the ultrathin BFO film, as shown by the dashed line in Fig. 3(d). The lattice rotation and the OOR extracted from the optimized atomic coordinates reveal nearly the same trend as the experimental results (Fig. 2(d) and (f)). The division between orthorhombic and rhombohedral phases could also be shown clearly by the ionic displacement mappings in the two directions. A difference between the experimental and calculated results is that the out-of-plane ionic displacements are larger than the in-plane ones in the experimental results while the calculated results show an opposite trend. The reason can be that the top surface of BFO film may adsorb some charged molecules which help screen the depolarization field and enhance the out-of-plane polarization. This effect was not considered in the first-principles calculations.

We also constructed a series of interface models which possess different ratios of the orthorhombic and rhombohedral parts in the BFO film, as shown in Fig. 4. The total energies of these models are

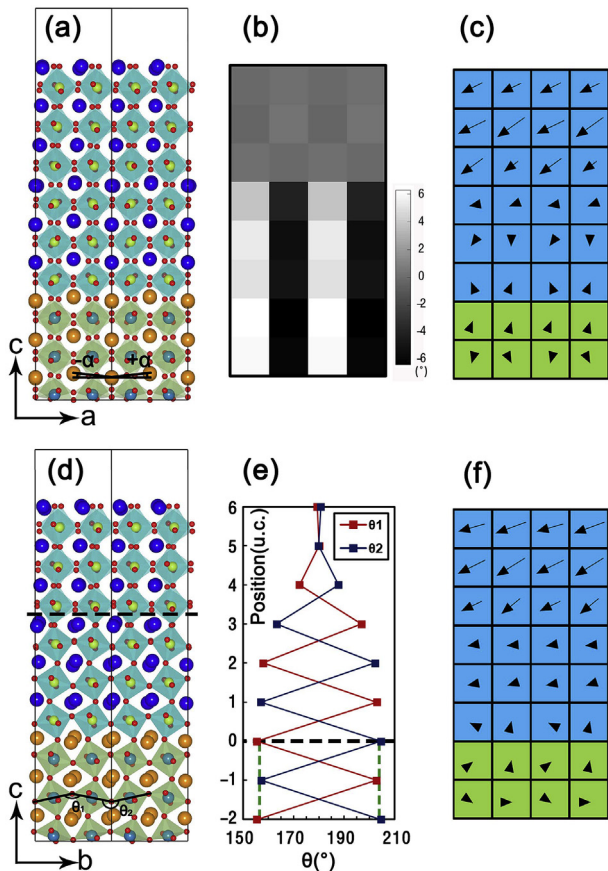


**Fig. 3.** First-principles calculation results of the BFO/NGO interface model. (a) The optimized atomic model projected in the  $b$ -axis. (b–c) The corresponding lattice rotation (angle  $\alpha$ ) mapping (b) and ionic displacement mapping (c). (d) The optimized atomic model projected in the  $a$ -axis. (e–f) The corresponding oxygen octahedron rotation (angle  $\theta$ ) distribution (e) and ionic displacement mapping (f).

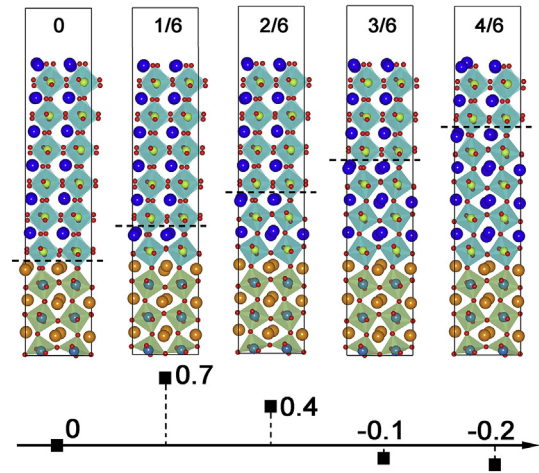


**Fig. 4.** The BFO/NGO interface models with different ratios of the orthorhombic and rhombohedral parts in the BFO film. The ratios are marked in the corresponding models and their relative energies are shown in the coordinate axis. The total energy of the first model is taken as the reference. The unit is eV.

shown. Taken the model with no orthorhombic part as the reference, the energies increase when one or two unit cells BFO are orthorhombic, indicating that these two systems are energetically unstable. When increasing the orthorhombic part of BFO into three or four unit cells, the energies become low and decrease into negative values, implying that the interfaces are more stable, which accords with the experimental results very well.

From the analysis above, we can conclude that BFO undergoes a phase transition from  $R3c$  to  $Pnma$  in about 3 unit cells at the BFO/NGO interface, whereas it still possesses the rhombohedral structure in the area near the surface. Several factors may induce the phase transition: strain, OOC, or both of them, according to the work of B. Carcan et al. [42].

To figure out which one is the main reason, we grew BFO ultrathin films on a series of orthorhombic substrates (DSO, GSO, NSO, and PSO) which exert different strains from compressive to tensile onto the BFO films, as shown in the axis in Fig. 5. The experimental results of the four interfaces are shown in Fig. 5(a–d). In each image, the upper left, upper right, lower left and lower right parts are the atomic resolved HAADF image along  $b$ -axis, the 2-D mapping of the Horizontal Lattice Rotation Angle ( $\alpha$ ), the ABF image along  $a$ -axis and the layer-position-dependent mean In-plane B–O–B Bond Angle ( $\theta$ ), respectively. From these images, we can tell that all of these heterostructures show similar distributions of the angles  $\alpha$  and  $\theta$ , no matter how the strain state of the BFO film is: tensile or compressive. A comparison with Fig. 2(c–f) tells us that the distributions at the four interfaces are nearly the same as the case of the BFO/NGO interface, which indicates that the phase transition from  $R3c$  to  $Pnma$  occur in all cases. Thus, epitaxial strain is not the cause of the phase transition at interface, while the crystal symmetry (i.e. OOR) plays the main role in this phase transition.

To give more solid evidence to the interfacial OOC, more structural parameters were chosen to reflect the structural similarity between the orthorhombic phases of the BFO films and the substrates for different strains. The In-plane and Out-of-plane B–O–B Bond Angle ( $\theta$  and  $\theta'$ ) and Horizontal Lattice Rotation ( $\alpha$ ) of the first two BFO unit cells above the interfaces and those of the substrates for films under different strains are comparatively shown in Fig. 6(a–c). It is found that the magnitudes of these structural parameters in films are very close to those in the substrates. A closer observation shows that  $\theta$  angles in the films are generally larger than those in the substrates, or closer to  $180^\circ$  as a consequence of

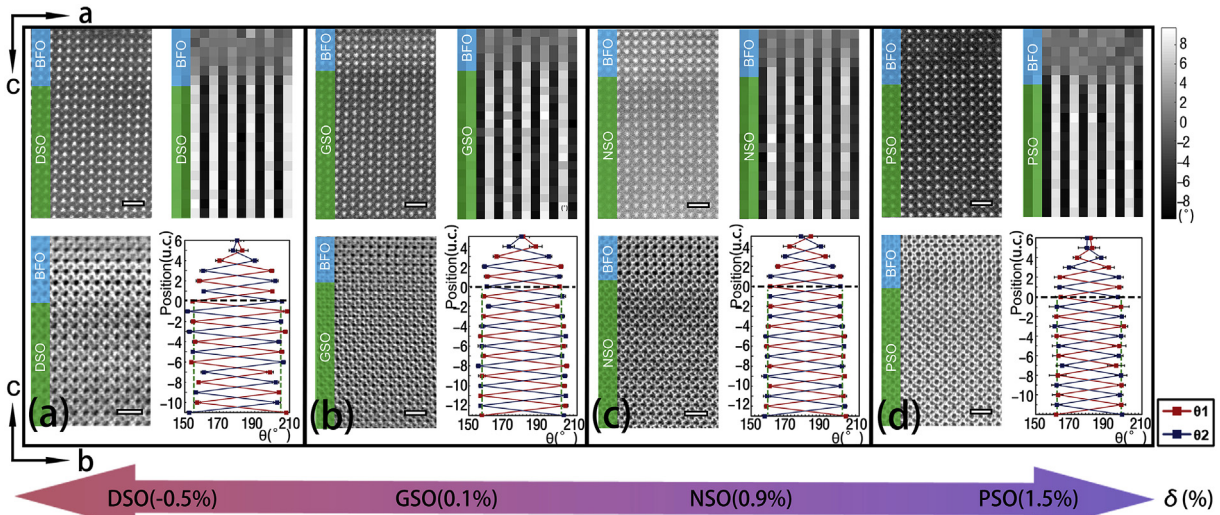


**Fig. 5.** Lattice and oxygen octahedral coupling at the BFO/DSO (a), BFO/GSO (b), BFO/NSO (c), and BFO/PSO (d) interfaces, from compressive to tensile strains. The upper left, upper right, lower left and lower right parts in each image are the atomic resolution HAADF image along *b*-axis, the 2-D mapping of the Horizontal Lattice Rotation ( $\alpha$ ), the ABF image along *a*-axis and the layer-position-dependent mean In-plane B-O-B Bond Angle ( $\theta$ ) of each heterostructure, respectively. The mismatch strains of BFO deposited on each substrate are shown in the coordinate axis. All scale bars denote 1 nm.

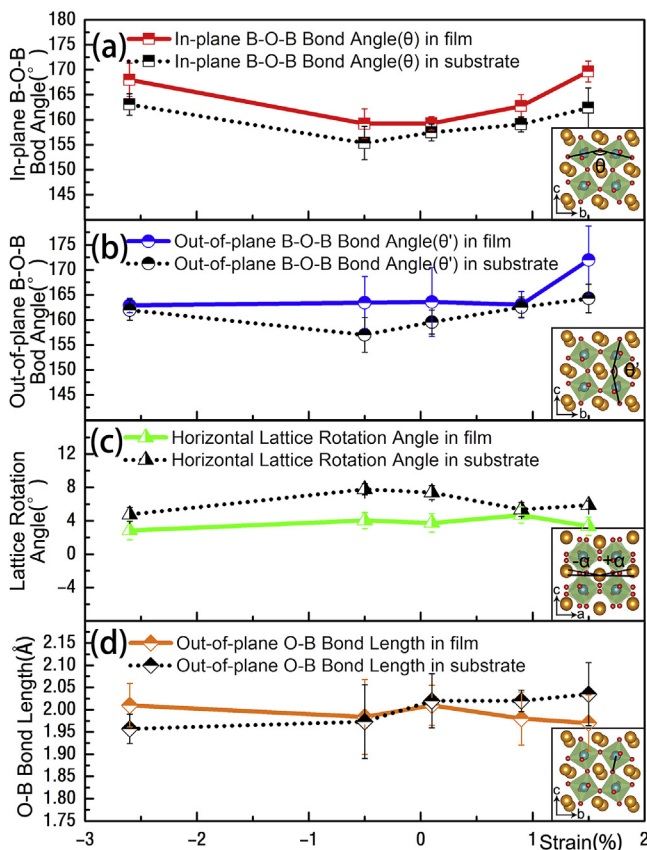


**Fig. 6.** Lattice and oxygen octahedral feature of BFO unit cells at interfaces with *Pnma* symmetry. (a) The In-plane B-O-B Bond Angle ( $\theta$ ), (b) the Out-of-plane B-O-B Bond Angle ( $\theta'$ ), (c) the Horizontal Lattice rotation ( $\alpha$ ) and (d) the Out-of-plane O-B Bond Length of BFO unit cells with *Pnma* symmetry under various strains. The insets are the sketches of these angles and length, respectively.

interfacial OOC (Fig. 6(a)). This behavior has already been shown in Fig. 2(f) and Fig. 5. As shown in Fig. 6(b),  $\theta'$  also shows a similar

behavior. Moreover,  $\alpha$  angles in the films are generally smaller than those in the substrates, as shown in Fig. 6(c). All these evidences strongly demonstrate that the substrates influence the films heavily through the interfacial OOC and this effect gradually diminishes away from the interface. To find out the influence of strain on BFO film in this system, we also calculated the Out-of-plane O-B Bond Length of BFO films for the first two BFO unit cells above the interfaces and those of the substrates, as shown in Fig. 6(d). The O-B Bond Length is enlarged under compressed strains, and decreased under tensile strains. This is easy to understand because the tensile strain tends to decrease the out-of-plane lattice parameter so that the Out-of-plane O-B Bond Length decreases at the same time, while compressive strain tends to enlarge the out-of-plane lattice parameter so that the Out-of-plane O-B Bond Length increases.

By now, the coexistence of rhombohedral and orthorhombic phases has been confirmed and it is very clear that the phase transition from *R3c* to *Pnma* is induced by OOC at interfaces. This *Pnma* phase of BFO has also been found in Sm-doped BiFeO<sub>3</sub> film [13–15] and BiFeO<sub>3</sub>/LaFeO<sub>3</sub> superlattice [42], where rare-earth doping is the main reason for the former case. In the latter case, the reason was ascribed by strain and crystal symmetry. Otherwise, this phase transition may appear in pure BFO when heated above  $T_c$  [43]. In our work, we demonstrated that crystal symmetry modulation itself can achieve phase transition from *R3c* to *Pnma* phase in BFO, while strain here is the reason for the changing in the O-B Bond Length in these heterostructures.

What should be paid attention to is that this crystal symmetry modulation is a short-range effect, the *Pnma* phase is only found in about 3–4 unit cells near interface, as shown in Fig. 2, while BFO still possess rhombohedral structure near surface, thus creating another kind of morphotropic phase boundary (MPB) [13,44–46] in this heterostructure. The coexistence of polar rhombohedral and non-polar orthorhombic was previously reported to have an enhanced piezoelectric response in samarium-substituted BFO films which originated from the electric-field-induced phase transition [15]. It was also reported that the phase transition from non-polar orthorhombic to polar rhombohedral is accompanied by a large volume expansion [43]. On this account, this kind of MPB construction we got may also have large piezoelectric response due

to the coupling of atomic polar displacements, oxygen octahedral rotations and strains when an electric field is applied. Hence, the enhancement of piezoelectric response may have many potential applications, such as ferroelectric sensors and actuators.

#### 4. Conclusion

In this study, we combined aberration-corrected high-resolution transmission electron microscopy and first-principles calculations to study the crystal structure of ultrathin BFO films grown on orthorhombic substrates. We found that three or four layers of BFO unit cells close to the substrate undergo a phase transition from ferroelectric *R3c* to paraelectric *Pnma*, while the BFO unit cells close to the surface still possess the rhombohedral structure, resulting in a two-phase coexistence. This kind of structure is similar to MPB and may have large piezoelectric response in the film and thus have potential utilization in ferroelectric sensors and actuators. The main reason for this phase transition was found to be the OOC between the substrate and the film. This work not only helps us better understand the OOC at heterostructure, but also offers us a promising pathway to the artificial design of heterostructures with multiple functionalities.

#### Acknowledgements

This work is supported by the National Natural Science Foundation of China (No. 51571197, 51231007, 51501194, 51401212 and 51671194), National Basic Research Program of China (2014CB921002), and the Key Research Program of Frontier Sciences CAS (QYZDJ-SSW-JSC010). Y. L. T. acknowledges the IMR SYNL-T.S. Kê Research Fellowship and the Youth Innovation Promotion Association CAS (No. 2016177). We are grateful to Mr. B. Wu and Mr. L.X. Yang of this lab for their technical support on the Titan platform of  $G^2$  60–300 kV aberration-corrected scanning transmission electron microscope.

#### References

- [1] J. Wang, J.B. Neaton, H. Zheng, V. Nagarajan, S.B. Ogale, B. Liu, D. Viehland, V. Vaithyanathan, D.G. Schlom, U.V. Waghmare, N.A. Spaldin, K.M. Rabe, M. Wuttig, R. Ramesh, Epitaxial BiFeO<sub>3</sub> multiferroic thin film heterostructures, *Science* 299 (2003) 1719–1722.
- [2] K.J. Choi, M. Biegalski, Y.L. Li, A. Sharan, J. Schubert, R. Uecker, P. Reiche, Y.B. Chen, X.Q. Pan, V. Gopalan, L.Q. Chen, D.G. Schlom, C.B. Eom, Enhancement of ferroelectricity in strained BaTiO<sub>3</sub> thin films, *Science* 306 (2004) 1005–1009.
- [3] D. Sando, A. Barthélémy, M. Bibes, BiFeO<sub>3</sub> epitaxial thin films and devices: past, present and future, *J. Phys. Condens. Matter* 26 (2014), 473201.
- [4] G. Catalan, J.F. Scott, Physics and applications of bismuth ferrite, *Adv. Mater.* 21 (2009) 2463–2485.
- [5] N.A. Spaldin, Multiferroics: past, present, and future, *MRS Bull.* 42 (2017) 385–389.
- [6] C. Michel, J.M. Moreau, G.D. Achenbach, R. Gerson, W.J. James, The atomic structure of BiFeO<sub>3</sub>, *Solid State Commun.* 7 (1969) 701–704.
- [7] F. Kubel, H. Schmid, Structure of a ferroelectric and ferroelastic monodomain crystal of the perovskite BiFeO<sub>3</sub>, *Acta Cryst B* 46 (1990) 698–702.
- [8] G.A. Smolenskii, I.E. Chupis, Ferroelectromagnets, *Sov. Phys. Usp.* 25 (1982) 475–493.
- [9] Z. Chen, Z. Luo, C. Huang, Y. Qi, P. Yang, L. You, C. Hu, T. Wu, J. Wang, C. Gao, T. Sritharan, L. Chen, Low-symmetry monoclinic phases and polarization rotation path mediated by epitaxial strain in multiferroic BiFeO<sub>3</sub> thin films, *Adv. Funct. Mater.* 21 (2011) 133–138.
- [10] P.M. Woodward, Octahedral tilting in perovskites. II. Structure stabilizing forces, *Acta Cryst B* 53 (1997) 44–66.
- [11] R.J. Zeches, M.D. Rossell, J.X. Zhang, A.J. Hatt, Q. He, C.H. Yang, A. Kumar, G.H. Wang, A. Melville, C. Adamo, G. Sheng, Y.H. Chu, J.F. Ihlefeld, R. Erni, C. Ederer, V. Gopalan, L.Q. Chen, D.G. Schlom, N.A. Spaldin, L.W. Martin, R. Ramesh, A strain-driven morphotropic phase boundary in BiFeO<sub>3</sub>, *Science* 326 (2009) 977–980.
- [12] Y.Y. Liu, L. Yang, J.Y. Li, Strain-engineered orthorhombic-rhombohedral phase boundary in epitaxial bismuth ferrite films, *J. Appl. Phys.* 113 (2013), 183524.
- [13] S. Fujino, M. Murakami, V. Anbusathaiah, S.H. Lim, V. Nagarajan, C.J. Fennie, M. Wuttig, L. Salamanca-Riba, I. Takeuchi, Combinatorial discovery of a lead-free morphotropic phase boundary in a thin-film piezoelectric perovskite, *Appl. Phys. Lett.* 92 (2008), 202904.
- [14] C.J. Cheng, D. Kan, S.H. Lim, W.R. McKenzie, P.R. Munroe, L.G. Salamanca-Riba, R.L. Withers, I. Takeuchi, V. Nagarajan, Structural transitions and complex domain structures across a ferroelectric-to-antiferroelectric phase boundary in epitaxial Sm-doped BiFeO<sub>3</sub> thin films, *Phys. Rev. B* 80 (2009), 014109.
- [15] D. Kan, L. Pálková, V. Anbusathaiah, C.J. Cheng, S. Fujino, V. Nagarajan, K.M. Rabe, I. Takeuchi, Universal behavior and electric-field-induced structural transition in rare-earth-substituted BiFeO<sub>3</sub>, *Adv. Funct. Mater.* 20 (2010) 1108–1115.
- [16] C.J. Cheng, A.Y. Borisevich, D. Kan, I. Takeuchi, V. Nagarajan, Nanoscale structural and chemical properties of antipolar clusters in Sm-doped BiFeO<sub>3</sub> ferroelectric epitaxial thin films, *Chem. Mater.* 22 (2010) 2588–2596.
- [17] C.L. Jia, M. Lentzen, K. Urban, Atomic-resolution imaging of oxygen in perovskite ceramics, *Science* 299 (2003) 870–873.
- [18] E. Okunishi, I. Ishikawa, H. Sawada, F. Hosokawa, M. Hori, Y. Kondo, Visualization of light elements at ultrahigh resolution by STEM annular bright field microscopy, *Microsc. Microanal.* 15 (2009) 164–165.
- [19] S.D. Findlay, N. Shibata, H. Sawada, E. Okunishi, Y. Kondo, T. Yamamoto, Y. Ikahara, Robust atomic resolution imaging of light elements using scanning transmission electron microscopy, *Appl. Phys. Lett.* 95 (2009), 191913.
- [20] D. Zhou, K. Müller-Caspary, W. Sigle, F.F. Krause, A. Rosenauer, P.A. van Aken, Sample tilt effects on atom column position determination in ABF-STEM imaging, *Ultramicroscopy* 160 (2016) 110–117.
- [21] Y.M. Kim, S.J. Pennycook, A.Y. Borisevich, Quantitative comparison of bright field and annular bright field imaging modes for characterization of oxygen octahedral tilts, *Ultramicroscopy* 181 (2017) 1–7.
- [22] C.L. Jia, L. Jin, D. Wang, S.B. Mi, M. Alexe, D. Hesse, H. Reichlova, X. Marti, L. Bellaiche, K.W. Urban, Nanodomains and nanometer-scale disorder in multiferroic bismuth ferrite single crystals, *Acta Mater.* 82 (2015) 356–368.
- [23] Q. He, R. Ishikawa, A.R. Lupini, L. Qiao, E.J. Moon, O. Ovchinnikov, S.J. May, M.D. Biegalski, A.Y. Borisevich, Towards 3D mapping of BO<sub>6</sub> octahedron rotations at perovskite heterointerfaces, unit cell by unit cell, *ACS Nano* 9 (2015) 8412–8419.
- [24] H.W. Eng, P.W. Barnes, B.M. Auer, P.M. Woodward, Investigations of the electronic structure of d<sup>0</sup> transition metal oxides belonging to the perovskite family, *J. Solid State Chem.* 175 (2003) 94–109.
- [25] Y. Wang, Y. Sui, P. Ren, L. Wang, X. Wang, W. Su, H.J. Fan, Correlation between the structural distortions and thermoelectric characteristics in La<sub>1-x</sub>A<sub>x</sub>CoO<sub>3</sub> (A = Ca and Sr), *Inorg. Chem.* 49 (2010) 3216–3223.
- [26] M. Kunz, I.D. Brown, Out-of-center distortions around octahedrally coordinated d<sup>0</sup> transition metals, *J. Solid State Chem.* 115 (1995) 395–406.
- [27] S. Pei, J.D. Jorgensen, B. Dabrowski, D.G. Hinks, D.R. Richards, A.W. Mitchell, J.M. Newsam, S.K. Sinha, D. Vaknin, A.J. Jacobson, Structural phase diagram of the Ba<sub>1-x</sub>K<sub>x</sub>BiO<sub>3</sub> system, *Phys. Rev. B* 41 (1990) 4126–4141.
- [28] J.M. Rondinelli, N.A. Spaldin, Substrate coherency driven octahedral rotations in perovskite oxide films, *Phys. Rev. B* 82 (2010), 113402.
- [29] Z. Liao, M. Huijben, Z. Zhong, N. Gauquelin, S. Macke, R.J. Green, S. Van Aert, J. Verbeeck, G. Van Tendeloo, K. Held, G.A. Sawatzky, G. Koster, G. Rijnders, Controlled lateral anisotropy in correlated manganite heterostructures by interface-engineered oxygen octahedral coupling, *Nat. Matters* 15 (2016) 425–431.
- [30] D. Kan, R. Aso, R. Sato, M. Haruta, H. Kurata, Y. Shimakawa, Tuning magnetic anisotropy by interfacially engineering the oxygen coordination environment in a transition metal oxide, *Nat. Matters* 15 (2016) 432–437.
- [31] J.M. Rondinelli, S.J. May, J.W. Freeland, Control of octahedral connectivity in perovskite oxide heterostructures: an emerging route to multifunctional materials discovery, *MRS Bull.* 37 (2012) 261–270.
- [32] A.Y. Borisevich, H.J. Chang, M. Huijben, M.P. Oxley, S. Okamoto, M.K. Niranjan, J.D. Burton, E.Y. Tsybmal, Y.H. Chu, P. Yu, R. Ramesh, S.V. Kalinin, S.J. Pennycook, Suppression of octahedral tilts and associated changes in electronic properties at epitaxial oxide heterostructure interfaces, *Phys. Rev. Lett.* 105 (2010), 087204.
- [33] R. Aso, D. Kan, Y. Shimakawa, H. Kurata, Atomic level observation of octahedral distortions at the perovskite oxide heterointerface, *Sci. Rep.* 3 (2013) 2214.
- [34] S.M. Anthony, S. Granick, Image analysis with rapid and accurate two-dimensional Gaussian fitting, *Langmuir* 25 (2009) 8152–8160.
- [35] C.L. Jia, V. Nagarajan, J.Q. He, L. Houben, T. Zhao, R. Ramesh, K. Urban, R. Waser, Unit-cell scale mapping of ferroelectricity and tetragonality in epitaxial ultrathin ferroelectric films, *Nat. Matters* 6 (2007) 64–69.
- [36] G. Kresse, J. Furthmüller, Efficient iterative schemes for ab initio total-energy calculations using a plane-wave basis set, *Phys. Rev. B* 54 (1996) 11169–11186.
- [37] J. Hafner, Materials simulations using VASP—a quantum perspective to materials science, *Comput. Phys. Commun.* 177 (2007) 6–13.
- [38] P.E. Blöchl, Projector augmented-wave method, *Phys. Rev. B* 50 (1994) 17953–17979.
- [39] Y. Yang, W. Ren, M. Stengel, X.H. Yan, L. Bellaiche, Revisiting properties of ferroelectric and multiferroic thin films under tensile strain from first principles, *Phys. Rev. Lett.* 109 (2012), 057602.
- [40] M. Raekers, K. Kuepper, S. Bartkowski, M. Prinz, A.V. Postnikov, K. Potzger, S. Zhou, A. Arulraj, N. Stüßer, R. Uecker, W.L. Yang, M. Neumann, Electronic and magnetic structure of RScO<sub>3</sub> (R=Sm,Gd,Dy) from x-ray spectroscopies and first-principles calculations, *Phys. Rev. B* 79 (2009), 125114.

- [41] A.M. Glazer, The classification of tilted octahedra in perovskites, *Acta Cryst B28* (1972) 3384–3392.
- [42] B. Carcan, H. Bouyanfif, M. El Marssi, F. Le Marrec, L. Dupont, C. Davoisne, J. Wolfman, D.C. Arnold, Phase diagram of BiFeO<sub>3</sub>/LaFeO<sub>3</sub> superlattices: antiferroelectric-like state stability arising from strain effects and symmetry mismatch at heterointerfaces, *Adv. Mater. Interfaces* (2017), 1601036.
- [43] M. Graf, M. Sepiarsky, S. Tinte, M.G. Stachiotti, Phase transitions and antiferroelectricity in BiFeO<sub>3</sub> from atomic-level simulations, *Phys. Rev. B* 90 (2014), 184108.
- [44] R. Maran, S. Yasui, E.A. Eliseev, M.D. Glinchuk, A.N. Morozovska, H. Funakubo, I. Takeuchi, V. Nagarajan, Interface control of a morphotropic phase boundary in epitaxial samarium modified bismuth ferrite superlattices, *Phys. Rev. B* 90 (2014), 245131.
- [45] A.Y. Borisevich, E.A. Eliseev, A.N. Morozovska, C.J. Cheng, J.Y. Lin, Y.H. Chu, D. Kan, I. Takeuchi, V. Nagarajan, S.V. Kalinin, Atomic-scale evolution of modulated phases at the ferroelectric-antiferroelectric morphotropic phase boundary controlled by flexoelectric interaction, *Nat. Commun.* 3 (2012) 775.
- [46] C.J. Cheng, D. Kan, V. Anbusathaiah, I. Takeuchi, V. Nagarajan, Microstructure-electromechanical property correlations in rare-earth-substituted BiFeO<sub>3</sub> epitaxial thin films at morphotropic phase boundaries, *Appl. Phys. Lett.* 97 (2010), 212905.